

The Mid-Atlantic Bight Cold Pool: The Slice Model

W. Brown and R. Arena
School for Marine Science and Technology
University of Massachusetts Dartmouth
706 S Rodney French Blvd.
New Bedford, MA 02744

Abstract

There is a general warming of the Mid-Atlantic Bight (MAB) Cold Pool of about 1°C per month from July through September. During September 2013, a three-glider fleet measured the warming. One question was how did the different oceanic processes warm the Cold Pool? To address the question, we developed a volume-averaged slice model of the Cold Pool temperatures of that warming. The temperature conservation model focused on the lower layer Cold Pool on a finite cross-shelf slice of the shelf. The volume-averaged temperature change of that slice is attributed to the (a) downward turbulent transport of temperature from the upper to the lower layer; convergence of advective temperature transport in the (b) long-shelf and (c) cross-shelf directions; and (d) turbulent temperature transport across the shelf-break front. We evaluated the model terms with nearly simultaneous ocean glider measurements at the northeastern, middle and southwestern sectors of the MAB. We found that during September 2013, the Cold Pool warming was relatively small, but consistent with the accepted overall 1°C per month warming of the MAB Cold pool waters. We also found that the upper layer warming of the lower layer Cold Pool was even order of magnitude smaller than our estimates of Cold Pool warming. The SNEB sector's *warming rate* $0.57^{\circ}\text{C}/\text{mo}$ was maintained by a competition between the onshelf advection (cross-SBF) of warm water across the seaward boundary and the *cooling* effects of the divergence of long-shelf flow. The onshelf warm water advection was part of the GS warm core ring's contribution. The New Jersey sector's negligible *warming rate* ($0.02^{\circ}\text{C}/\text{mo}$) was maintained by a near-balance between the robust *cooling* associated with the divergence of long-shelf advective temperature transport and the robust *warming* of the onshelf eddy temperature transport. The onshelf advective temperature transport was less important to the balance than the SNEB region. The Maryland sector's *warming rate* ($1.07^{\circ}\text{C}/\text{mo}$) – the largest in the MAB during September 2013 - was maintained by the robust *warming* effects of the long-shelf advective temperature transport convergence and opposed by the robust *cooling* effects from the offshelf advective temperature transports.

I. THE MISSION

During September and October 2013, MARACOOS organized a 9-glider deployment consisting of operations all along the American coastal ocean between Nova Scotia and Florida - *GliderPalooza 2013*. Here we focus on a four-glider subset of missions in the Middle Atlantic Bight (MAB; see Figure 1). The gliders BLUE, RU23 and RU22 missions were almost simultaneous. In addition, RU28 patrolled the inner shelf in water depths less than 30m along the NJ coast at the same time. Three of these gliders also tested the hypothesis that triangular patterns are particularly effective for data-assimilation numerical modeling of MAB flow with a general 5 km/day southwestward flow.

Glider Blue traced out a near-equilateral triangular trajectory. During its transit of Leg-2, glider Blue sliced through the Cold Pool twice (see Figure 1); penetrating the shelf-break front (SBF) during its outgoing and incoming legs. Almost simultaneously, glider RU23 sliced through the Cold Pool twice - extending beyond the SBF - during its right triangular trajectory off the New Jersey coast. A week or so later, glider RU22 also penetrated the SBF, as it sliced through the Cold Pool twice (see Brown et al., 2020).

II. Water Property Measurements

This trio of gliders measured water temperatures (and other water properties) almost at the same times in different parts of the Mid-Atlantic Bight (MAB). Figure 1 shows that transect-minimum temperatures T_{min} are clustered near the shelf break all along the MAB. This figure also shows that in September 2013 there was (a) the MAB's

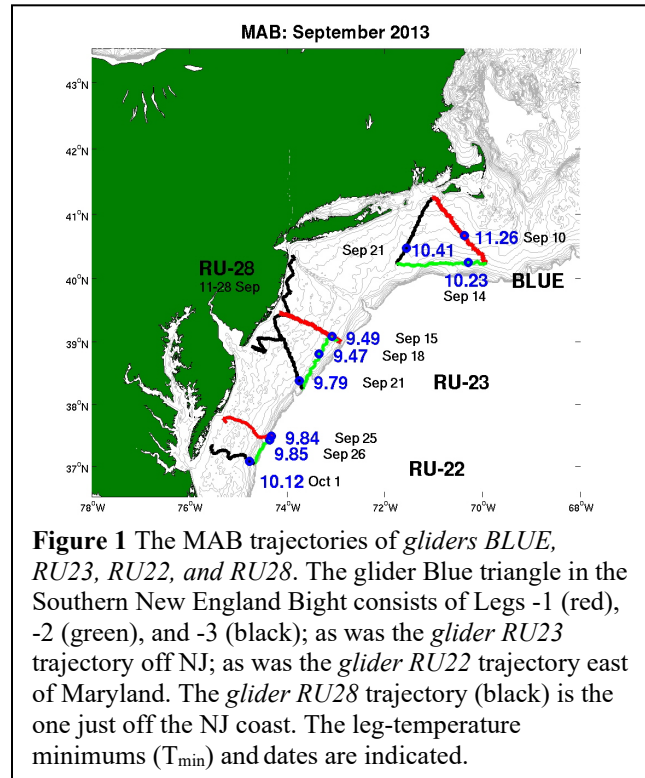


Figure 1 The MAB trajectories of *gliders BLUE, RU23, RU22, and RU28*. The glider Blue triangle in the Southern New England Bight consists of Legs -1 (red), -2 (green), and -3 (black); as was the *glider RU23* trajectory off NJ; as was the *glider RU22* trajectory east of Maryland. The *glider RU28* trajectory (black) is the one just off the NJ coast. The leg-temperature minimums (T_{min}) and dates are indicated.

Table 1 The average temperatures of the Sep.-Oct. 2013 waters with temperatures greater than 12°C (upper) and less than 12°C (lower); section-minimum temperatures T_{min} and associated salinities S_{Tmin} also p.

Glider Sec. ID	Dates SEP 2013	Upper Layer Ave. T(°C)	Lower Layer Ave. T(°C)	T_{min} (°C)	S_{Tmin} (psu)
BLUE					
Leg-1	06-13	16.40	11.11	10.32	33.33
Leg-2	13-19	16.87	11.25	10.23	33.38
Leg-3	19-26	16.22	11.38	10.41	33.45
AVE	16	16.50	11.25	10.31	33.39
RU23					
Leg-1	10-15	20.10	10.52	9.48	33.48
Leg-2	15-20	18.62	10.07	9.46	33.43
Leg-3	20-27	18.62	10.54	9.79	33.47
AVE	19	19.11	10.38	9.58	33.46
RU22					
Leg-1	12-26	19.12	10.74	9.84	33.35
Leg-2	26-30	17.75	10.72	9.85	33.36
Leg-3	S30-O16	19.23	11.20	10.12	33.43
AVE	29	18.70	10.89	9.94	33.38

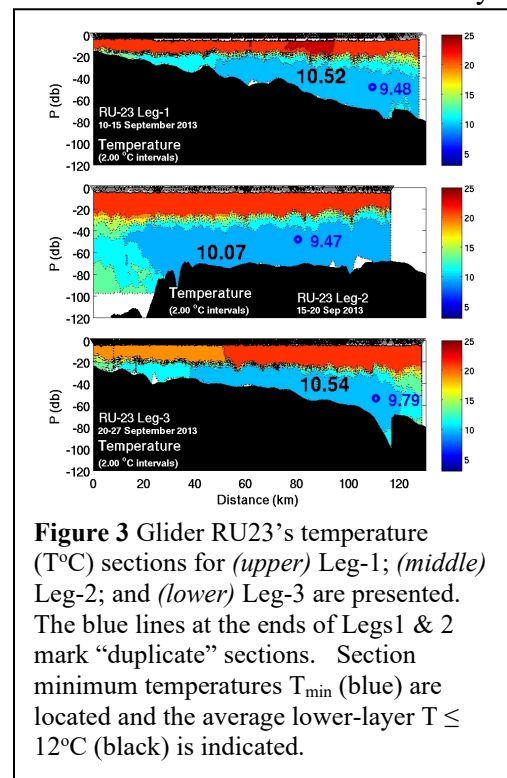
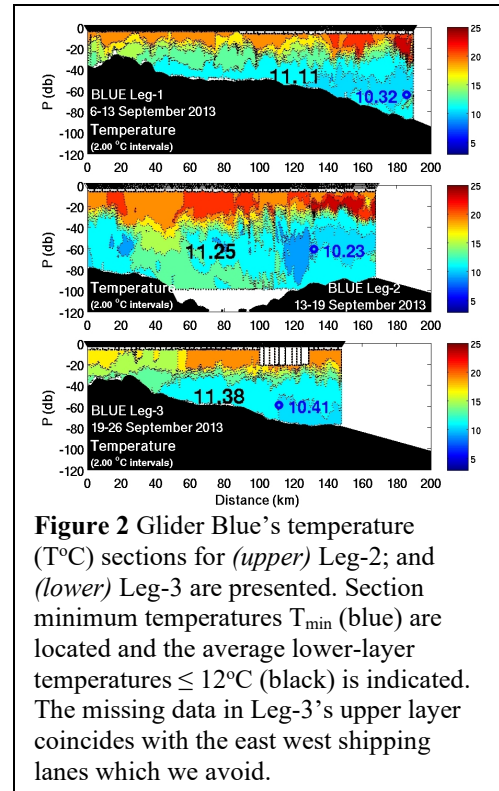
coldest water off New Jersey; and (b) no sub-10°C in the Southern New England Bight (SNEB) region of the MAB (also see Table 1). Because there was a distinct Cold Pool signature in the SNEB waters (see Figure 2), we chose to define the Cold Pool by the 12°C isothermal surface.

The glider Blue temperature sections measured in SNEB clearly show a two-layered structure (see Figure 2); the layers separated by the 12°C isotherm (aliased internal tidal wave activity contributes to the ragged look of the thermocline). The SNEB lower-layer temperatures ($\leq 12^\circ\text{C}$) along Leg-1 average $11.11 \pm 0.04^\circ\text{C}$; and along Leg-3 average $11.38 \pm 0.04^\circ\text{C}$, respectively (Table 1). The task is to define the boundaries of the sub-12°C Cold Pool waters.

These Leg-1 and -3 measurements indicate that the sub-12°C Cold Pool goes inshore to about the 50db isobath. During its Leg-2, glider Blue sliced through the 12°C Cold Pool's offshore boundary both going offshore and onshore (see Figure 2- middle panel). During the offshore part of Leg-2, the 12°C Cold Pool extended offshore 40km beyond the 100db isobath. During the onshore part of Leg-2, glider measurements show the 12°C Cold Pool extended only to the 80db isobath. We attribute this asymmetry in the extent of the Cold Pool waters to the influence of the Gulf Stream Warm Core Ring.

The ocean dynamics at the New Jersey (NJ) shelf-break were quite different (see Figure 3). Glider RU23 was measuring a well-defined 12°C Cold Pool seaward of NJ also, but the NJ Cold Pool waters were colder (average 10.38°C - Table 1) than the SNEB Cold Pool waters (average 11.24°C). In fact, the coldest part of the September 2013 12°C Cold Pool was off NJ. The geography of the NJ Cold Pool was defined by an inshore boundary that in relatively shallow 20m waters (according to Leg-1 and -3 glider measurements - Figure 3). Unfortunately, glider RU-23 did not go far enough seaward to measure the 12°C Cold Pool's offshore boundary.

RU22 measured a much narrower 12°C Cold Pool off Maryland (MD) than it was off New Jersey (see Figure 4/Table 1). The inshore boundary of the 12°C Cold Pool was near the 40m isobath on a much narrower part of



the MAB shelf. Unfortunately like RU23, RU22 did not go far enough seaward to measure this 12°C Cold Pool's *offshore boundary*. It is perhaps a large distance beyond the 100m isobath as suggested by the results presented later.

In summary, this trio of glider measurements appears to have crudely defined the extent of the MAB Cold Pool in September-October 2013. The sub-12°C Cold Pool's inshore boundaries and offshore boundaries and are indicated in Figure 5. They were used to construct a bottom footprint of the MAB sub-12°C waters as indicated in pink. If we assume an average upper layer thickness of 25m, the sub-12°C waters fill a volume of 4093 km³. In the next section, we address the question.

What do the glider-measured currents suggest about the observed differences in water temperature and geographical configuration of the September-October 2013 MAB Cold Pool? In Section IV below, we address the question ... What are the relative roles and magnitudes of the different oceanic processes that warm/cool the Cold Pool locally during the summer? But first, we first we describe the current field which the gliders measure.

III. Currents

Every time a Slocum glider completes an underwater segment, it surfaces and obtains a GPS location. This enables the glider computer to compute the average ocean current that was needed to deflect the glider from its dead-reckoned position (Stommel, 1989) as it travelled over that segment.

Glider Blue's September 2013 trajectory three-hourly average current vectors time series was detided as described by Brown et. al, 2020. That de-tiding process resulted in a time/space current series with subtidal fluctuations with periods greater than a couple of days. These glider Blue hourly subtidal current series consist of (a) relatively small flows (~ 1 cm/s) along most of Leg-1 until the end (see Figure 6); (b) Leg-2 has much stronger 10 cm/s northwestward (landward) flows; and (c) Leg-3 has relatively strong (~10 cm/s) northwestward (landward) flows along.

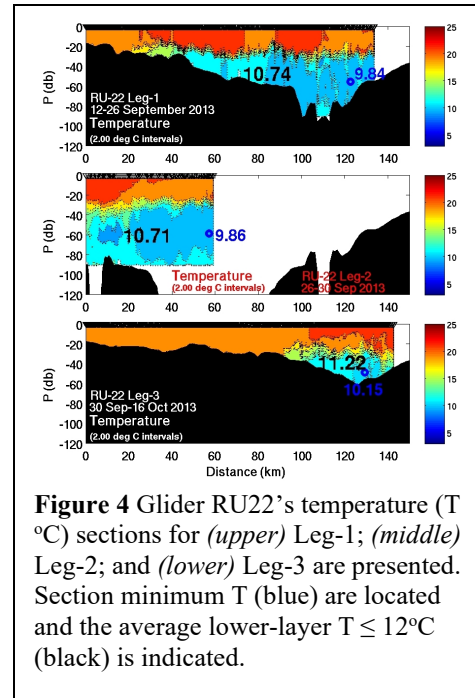


Figure 4 Glider RU22's temperature (T °C) sections for (upper) Leg-1; (middle) Leg-2; and (lower) Leg-3 are presented. Section minimum T (blue o) are located and the average lower-layer T ≤ 12°C (black) is indicated.

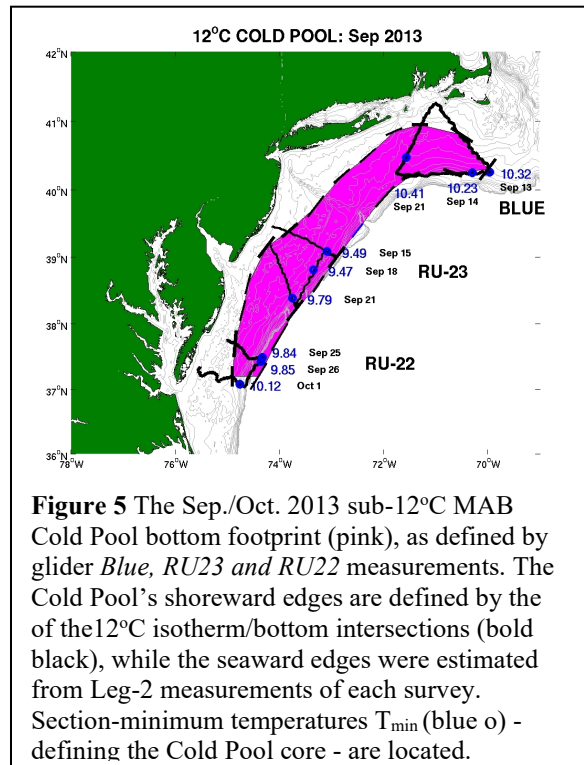
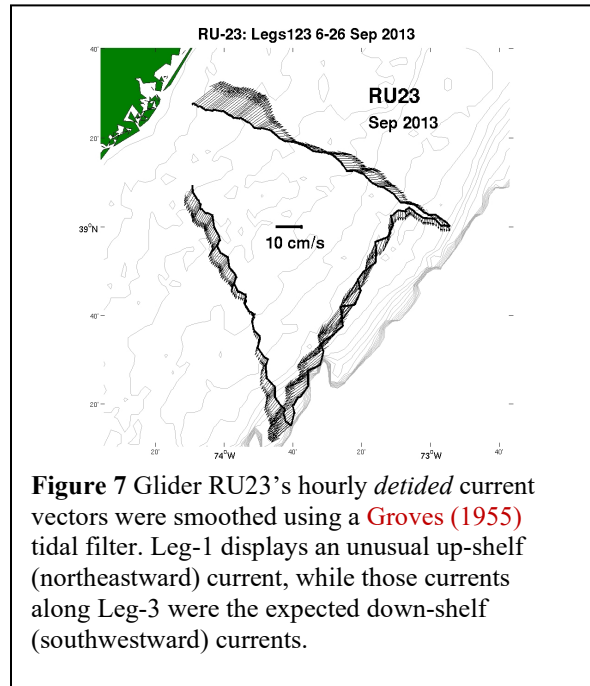
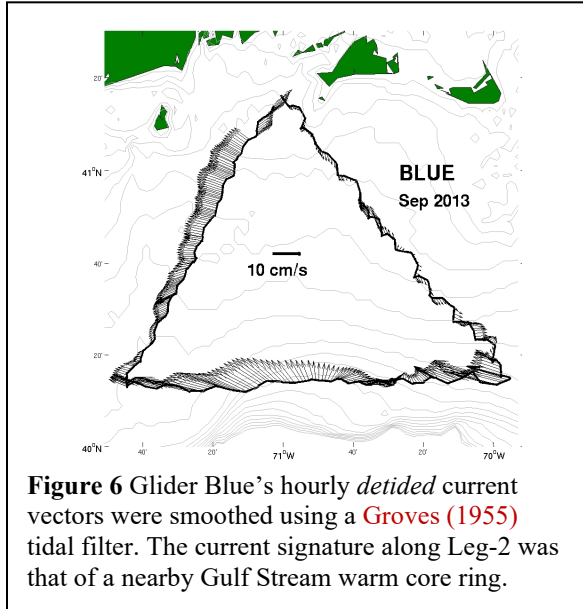


Figure 5 The Sep./Oct. 2013 sub-12°C MAB Cold Pool bottom footprint (pink), as defined by glider Blue, RU23 and RU22 measurements. The Cold Pool's shoreward edges are defined by the of the 12°C isotherm/bottom intersections (bold black), while the seaward edges were estimated from Leg-2 measurements of each survey. Section-minimum temperatures T_{min} (blue o) - defining the Cold Pool core - are located.



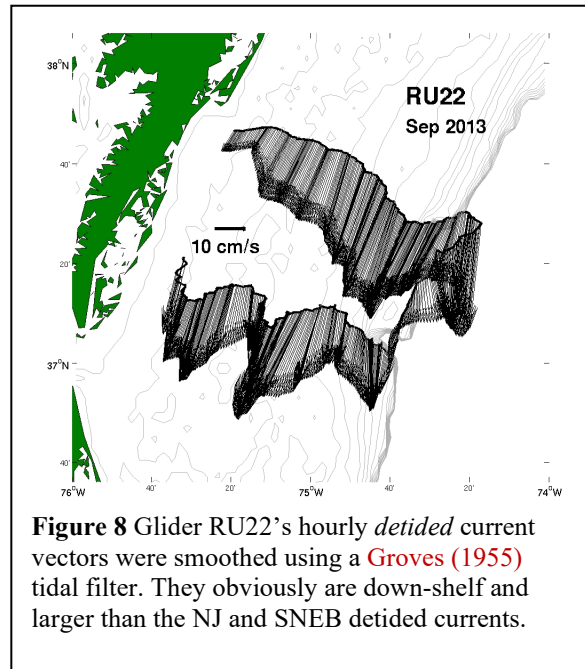
The hourly, section-averaged, non-tidal currents for the NJ (RU-23) and MD (RU-22) regions are presented in Figures 7 and 8, respectively. The NJ glider-current domain features alongshelf divergence with predominantly up-shelf currents along Leg-1 and down-shelf currents along Leg-3. The MD glider-current domain features much larger currents; presumably because of the narrowing of the as one southwestward in the MAB. The MD long-shelf currents converge to feed the exiting Cold Pool water.

In what follows in Section VI, we develop and apply the theoretical framework of the Cold Pool Slice Model to the problem of the warming of the Cold Pool waters during September 2013.

IV. Cold Pool Temperature Conservation Model

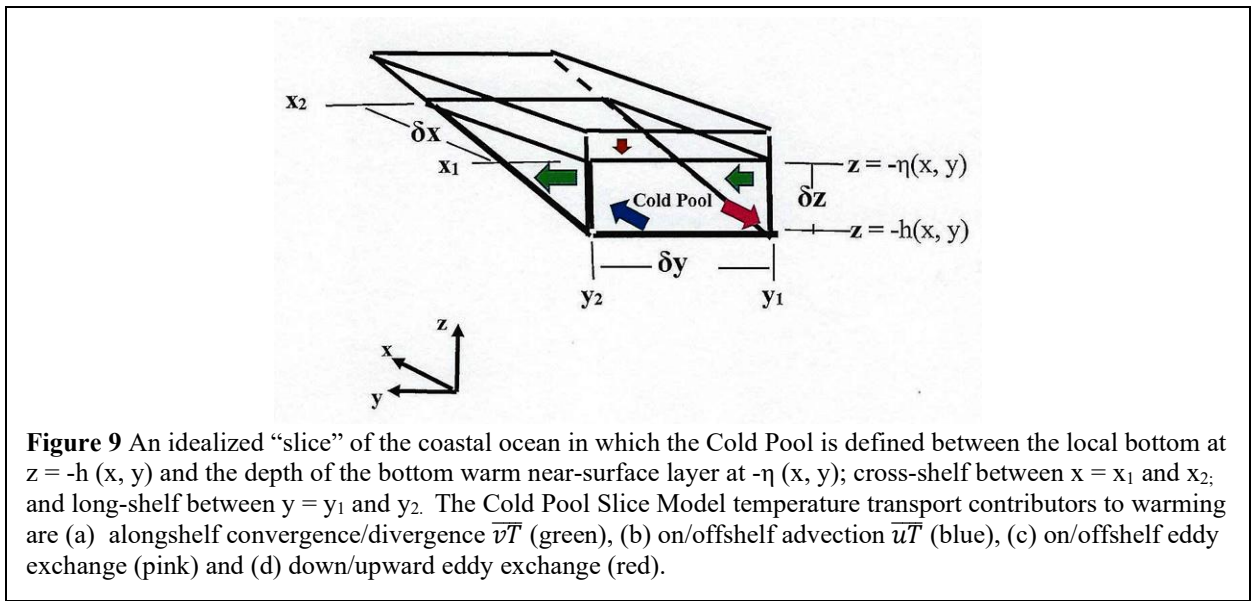
Here we develop a model on the temperature energetics in the Cold Pool that is eventually evaluated with ocean glider measurements. We start with the Landhl and Mollo-Christensen (1992) mean turbulent heat flux equation

$$\rho_o C_p \left(\frac{\partial \bar{T}}{\partial t} + \bar{u} \frac{\partial \bar{T}}{\partial x} + \bar{v} \frac{\partial \bar{T}}{\partial y} + \bar{w} \frac{\partial \bar{T}}{\partial z} \right) = \frac{\partial}{\partial x_i} \left(k \frac{\partial \bar{T}}{\partial x_i} - \rho_o C_p \overline{u_i T'} \right), \quad (1)$$



where $\rho_o (=1025 \text{ kg/m}^3)$ is the reference density, $C_p (= 3990 \text{ Ws/kg } ^\circ\text{C})$ is the seawater heat capacity, $k = \rho_o C_p \kappa$ is the molecular thermal conductivity with the molecular thermal diffusivity $\kappa (= 1.5 \times 10^{-7})$, and that turbulent $\rho_o C_p \overline{u_i T'}$ can be approximated by $K_i (-\partial \overline{T} / \partial x_i)$ with the turbulent thermal conductivity K_i in the respective directions. Then we integrate Eq. (1) spatially over a simplified conceptual model of a slice of the Cold Pool in [Figure 9](#) and over a finite time δt ; typically a couple weeks.

We consider the (1) turbulent temperature transport (a proxy for heat) from the warm upper layer to the cold lower layer; (2/3) convergence (divergence) of long- and cross-shelf temperature transport; and (4) turbulent temperature transport. We assume that the long-shelf turbulent temperature transport is negligibly small relative to advective transport.



The integration of Eq. (1) gives the following Cold Pool Slice Model (CPSM) temperature conservation statement (see [Appendix A](#) for details):

$$\frac{\delta \overline{T}_{ave}}{\delta t} = \underbrace{-\frac{2}{\delta x} K_x \frac{\partial \overline{T}}{\partial x}(x_1)}_{Term-1} + \underbrace{\frac{2}{\delta x} \overline{uT}(x_1)}_{Term-2} + \underbrace{\frac{2}{\delta y} \left((\overline{vT}(y_1)) - (\overline{vT}(y_2)) \right)}_{Term-3} + \underbrace{\frac{2}{\delta z(x_1)} K_z \frac{\partial \overline{T}}{\partial z}(-\eta)}_{Term-5} \quad (2)$$

-----Term-4-----

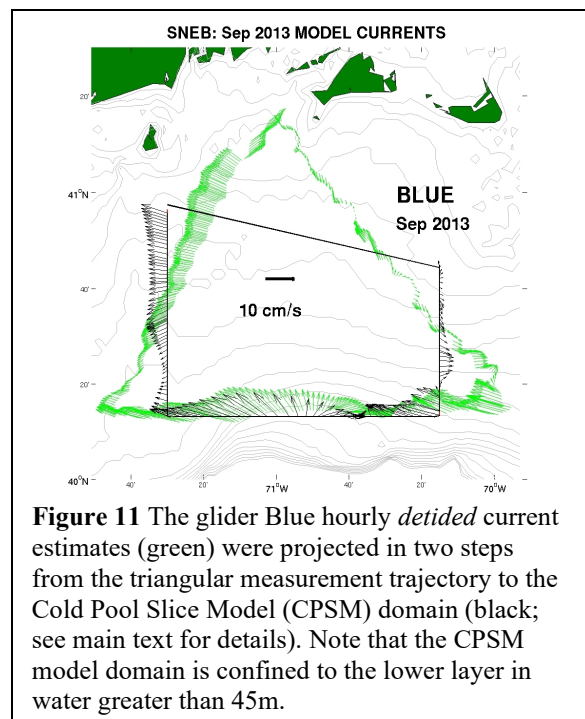
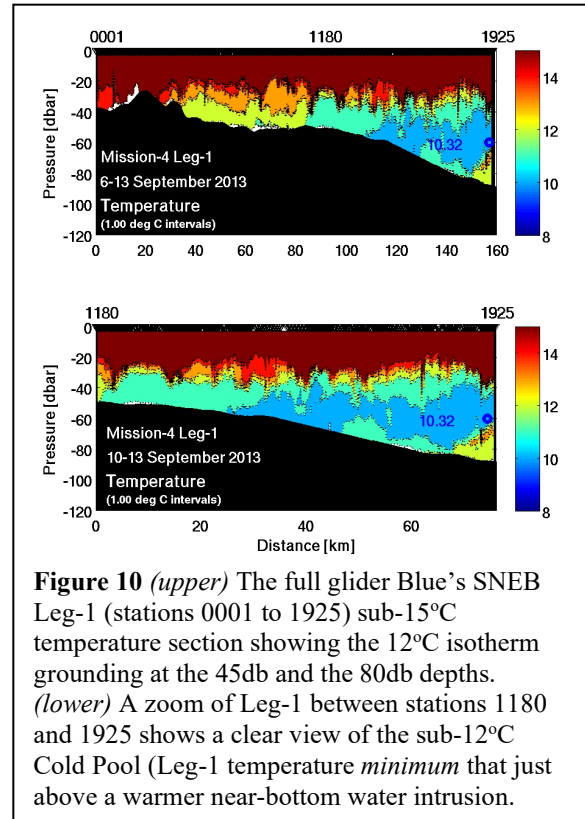
Term-1 of Eq. (2) is the average time-rate change of the domain volume-averaged temperature in terms of the contributions of the right-hand-side terms. *Term-2* is the onshelf/offshelf turbulent (or eddy) temperature transport through the seaward boundary. *Term-3* is the on/offshelf advective temperature transport through the seaward boundary. *Term-4* is the convergence/divergence of the long-shelf advective temperature transport based on the difference of the temperature transports through the up and down-shelf sections at y_1 and y_2 , respectively. *Term-5* is the downward/upward eddy temperature transport at the base of the thermocline.

V. Model Application

The CPSM was first applied to the Southern New England Bight (SNEB) region of the MAB. The CPSM Eq. (2) terms were estimated using glider Blue's data (see Figure 1) and other considerations as described below. We define the Cold Pool these September 2013 glider observations by the 12°C isotherm. The sub-12°C waters of the SNEB Cold Pool in the Leg-1 section are defined by the 12°C isotherm (see the green/yellow boundary in Figure 10). On the inshore side, the 12°C isotherm intersects the bottom at about the 45 m isobath at station 1180. On the offshore side, the 12°C isotherm intersects the bottom at about the 80 m isobath. Along Leg-3 the 12°C isotherm intersects the bottom at about the 45 m isobath at station 3861. The geography of the SNEB CPSM domain is shown in Figure 11.

We project the glider-acquired currents and water properties, first along the three straight-line legs of the triangle. Then we project the straight-line currents and water properties onto the geometry of the Cold Pool Slice Model (CPSM; see Figure 11). Specifically, the Cold Pool currents and temperatures between stations 1180 and 1925 along Leg-1 are projected onto the north-south Leg-1 (70.25°W) depicted in Figure 11. Likewise the glider-acquired data between (a) stations 1925 and 2757 along Leg-2 are projected along the east-west segment (40.22°N); and (b) between stations 2757 and 3861 were projected the other north-south CPSM Leg-3 (71.5°W). These vertical boundary sections and the CPSM's ceiling - the depth at the 12°C isotherm ($z = -\eta$) and the bathymetry [$z = -h(x,y)$] - define the shape of the model domain. Note that for the SNEB-region, the inshore CPSM boundary is consistent with a Cold Pool that extends to the 45 m isobath. It is over this CPSM domain that the terms in Eq (2) are estimated from glider Blue terms.

The SNEB region's warming rate (*Term-1* in Eq. (2)) was estimated to be $0.57 \pm 0.16^\circ\text{C}$ per 30.25-day month estimate (see Table 2). The Cold Pool warming rate by dividing the difference of



respective average sub-12°C temperatures of Leg-3 ($11.38 \pm 0.11^\circ\text{C}$) and Leg-1 ($11.11 \pm 0.11^\circ\text{C}$) see [Figure 2](#); [Table 1](#)) by 2 weeks - the typical glider transit time between the mid-points of Legs-1 and -3. The warming rates of the for the NJ and MD regions were estimated to be $0.02 \pm 0.16^\circ\text{C}/\text{mo}$ and the $1.07 \pm 0.16^\circ\text{C}/\text{mo}$, respectively. While these small warming rates differ significantly, they all are consistent with $1^\circ\text{C}/\text{mo}$ overall summer warming rate of the Cold Pool.

Table 2 The Cold Pool Slice Model application summary of Eq. (2) term estimates ($^\circ\text{C}/\text{month}$) using with glider data from different sectors of the MAB. The *Term-2* values were derived by assuming a balance in the warming rate budget for each sector.

$$\frac{\delta\bar{T}_{ave}}{\delta t} = -\frac{2}{\delta x}K_x\frac{\partial\bar{T}}{\partial x}(x_1) + \frac{2}{\delta x}\bar{u}\bar{T}(x_1) + \frac{2}{\delta y}\left(\bar{v}\bar{T}(y_1) - \bar{v}\bar{T}(y_2)\right) + \frac{2}{\delta z(x_1)}K_z\frac{\partial\bar{T}}{\partial z}(-\eta)$$

	<i>Term-1</i>	<i>Term-2</i>	<i>Term-3</i>	<i>Term-4a</i>	<i>Term-4b</i>	<i>Term-4</i>	<i>Term-5</i>
SNEB	0.57 ± 0.16	-14.10	35.77	5.58	-26.84	-21.26	0.16 ± 0.02
<i>BLUE</i>	net warming	cooling	warming	warming	cooling	cooling	weak warming
NJ	0.02 ± 0.16	37.26	11.23	-12.75	-35.78	-48.53	0.06 ± 0.02
<i>RU23</i>	net warming	warming	warming	cooling	cooling	cooling	weak warming
MD	1.07 ± 0.16	18.11	-119.90	303.50	-200.70	102.80	0.06 ± 0.02
<i>RU22</i>	net warming	warming	robust cooling	warming	cooling	robust warming	weak warming

The SNEB region’s downward eddy temperature transport into the Cold Pool (*Term-5* in Eq. (2)) was estimated to be a relatively small warming rate of $0.16 \pm 0.02^\circ\text{C}/\text{mo}$, using the [Lentz \(2017\)](#) climatological estimates for K_z and dT/dz (see [Table 3](#)). The downward eddy warming rates (*Term-5*) for the NJ and MD sectors were smaller than that for the SNEB region and, as we will see below are at least an order of magnitude less than the other Eq. (2) right-hand-side terms. How did we estimate the larger terms?

Table 3 Summary of the estimates of the Eq. (2) downward turbulent heating term $K_z(\partial\bar{T}/\partial z)/\delta z \cdot (1 \& 2; \text{ see } \text{Lentz, 2017})$

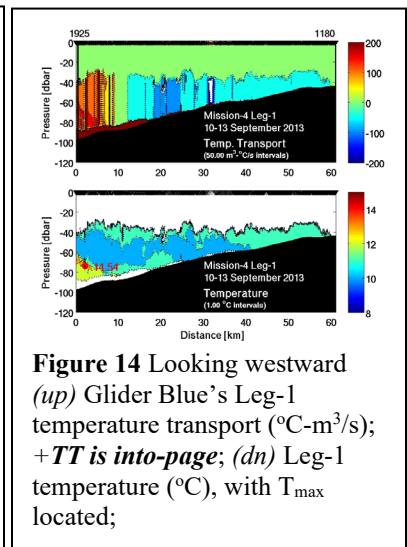
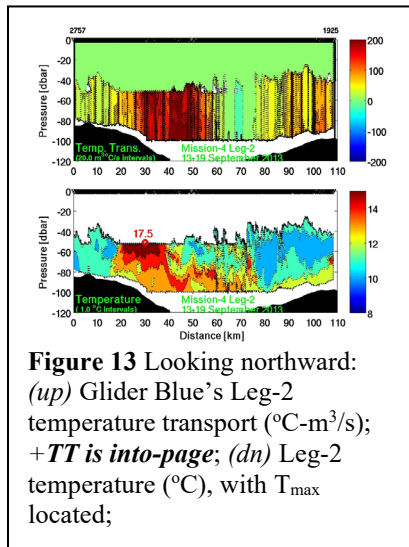
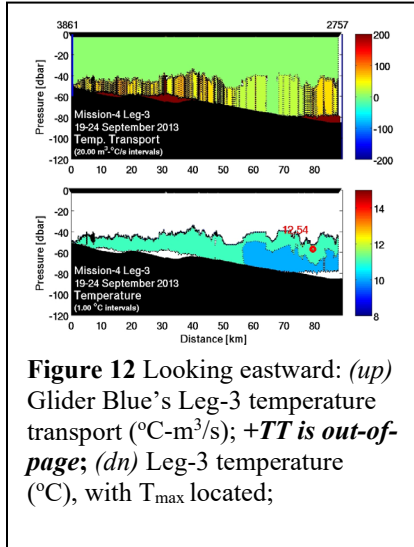
Glider	$\frac{\partial\bar{T}}{\partial z}$ ($^\circ\text{C}/\text{m}$)	K_z (m^2/s)	Estimates ($^\circ\text{C}/\text{s}$)
BLUE	0.25	10^{-5}	0.06×10^{-6}
RU-23	0.45	10^{-6}	0.02×10^{-6}
RU-22	0.45	10^{-6}	0.02×10^{-6}

Table 4 The Cold Pool Slice Model application geographical data δx , δy , δz and leg-averaged velocities.

Param/ID	<i>BLUE</i>	<i>RU-23</i>	<i>RU-22</i>
δz (m)	50	67	57
δy (m) (leg-2)	106.0×10^3	79.1×10^3	53.9×10^3
δx (m) ave.	75.2×10^3	106.3×10^3	43.1×10^3
(leg-1 δx)	61.4×10^3	87.7×10^3	59.4×10^3
(leg-3 δx)	89.0×10^3	124.9×10^3	26.7×10^3
$\bar{v}(y_1)$ (m/s)	0.006	-0.049	0.264
$\bar{u}(x_1)$ (m/s)	0.036	0.016	-0.049
$\bar{v}(y_2)$ (m/s)	0.046	0.045	0.232
orient ($^\circ\text{T}$)	0	-63	-72

The CPSM TT distributions for the three sections of the SNEB region are presented for the reader who is looking (a) eastward at Leg-3 ([Figure 12](#)); (b) northward at Leg-2 ([Figure 13](#)); and (c) westward at Leg-1 ([Figure 14](#)), respectively. The Leg-1 TT section ([Figure 14](#)) exhibits a weak eastward (negative) TT in the shallower ends of the section. At the deeper end of the Leg-1 section there is a robust westward (positive) TT.

The net Leg-1-average TT per unit cross-section area is a westward 0.2336 ± 0.02 °C-m/s. This contrasts with Leg-3 that has a section-average TT of a more robust westward 1.0869 ± 0.10 °C-m/s. We convert TT into warming rates by dividing by the appropriate Table 4 geometrical factor. The SNEB longshelf TT divergence translates to a *Term-4* robust cooling tendency of -8.05×10^{-6} °C/s (-21.26 °C/mo; see Table 2). This longshelf TT divergence is compensated by a more variable Leg-2 advective TT that averages to northward 1.0204 °C-m/s (see Figure 13). Note the slug of warm water flowing through the Leg-2 lower layer onto the shelf in Figure 13.



The glider Blue – advective warming rate across CPSM’s seaward boundary - was estimated to be 13.6170×10^{-6} °C/s (or *Term-3* = $+35.77$ °C/mo); using the SNEB region Leg-2 TT from above multiplied by the geometrical factor $2/\delta x$ (see Table 2).

The estimate of the *Term-2* eddy temperature transport across the seaward boundary was the most uncertain term in Eq. (2). Therefore, we estimated *Term-2* on the basis of an assumed overall balance. Thus our estimate of the eddy exchange between the shelf and the slope sea waters across the Leg-2 transect is the sum of our estimates of Eq. (2) *Terms-3, -4, -5* and *-1* estimates of Eq. (3) accordingly

$$\frac{2K_x}{\delta x} \frac{\partial \bar{T}}{\partial x}(x_1) = \frac{2}{\delta x} \overline{uT}(x_1) + \frac{2}{\delta y} \left((\overline{vT}(y_1)) - (\overline{vT}(y_2)) \right) + \frac{2}{\delta z(x_1)} K_z \frac{\partial \bar{T}}{\partial z}(-\eta) - \left(\frac{\delta [\bar{T}]_{ave}}{\delta t} \right). \quad (3)$$

Term-2
Term-3
Term-4
Term-5
Term-1

Thus, the estimate Eq. (2) *Term-2* onshelf eddy exchange of temperature between the shelf Cold Pool and the Slope Sea waters for the SNEB region is a cooling rate of 14.10 °C/mo; for the NJ region *Term-2* is robust warming rate of 37.26 °C/mo; twice that for the MD region (see Table 2). This diversity of eddy exchange results is consistent with the overall CPSM results for each region, which are graphically presented for each region in Figures 15, 16 and 17, respectively. Each of these sub-regions differs from SNEB in terms of the processes that support warming rates in these different MAB regions. See Appendix B for a discussion of the 95% uncertainty limits that characterize the terms that involve the glider-measured velocities.

For example, the NJ region in September 2013 is warming at a lower rate than SNEB and MD. The SNEB regional warming rate is due primarily to the near-balance of the (a) alongshelf advection divergence (green) and (b) onshelf advection (blue); aided by some offshelf eddy cooling. This is a specific case where a passing GS warm core eddy is contributing to the warming of the Cold Pool (see Figure 18).

The regional NJ alongshelf divergence is larger than the SNEB region because of unusually persistent northeastward currents during the time RU-23 was transiting Leg-1 (see Figure 16). It is most likely that these currents were caused by the northeastward 10 m/s winds that Tremblay (2019) documents at the offshore buoys between 9 and 14 September 2013. On the shoreward Leg-3 RU-23 measured a persistent southwestward current (see Figure 16). The larger long-shelf divergence had a robust cooling effect that was nearly balanced by a significant onshelf eddy warming. Perhaps GS warm core eddy (see Figure 18) destabilized the shelf/slope front off New Jersey in September 2013.

The regional MD shelf was the hotspot of action – partly because the MAB shelf narrows there. The narrowing shelf combines with the proximity of the Gulf Stream to force part of the warming Cold Pool offshore in this sector of the MAB. That locale was being warmed (1.07 °C/mo) in September 2013 more rapidly than the two other regions. This very robust alongshelf/offshelf temperature advection is 5 times more energetic than the other regions; and despite the large cooling accompanying a robust offshelf advection of temperature (see Figure 17/Table 2).

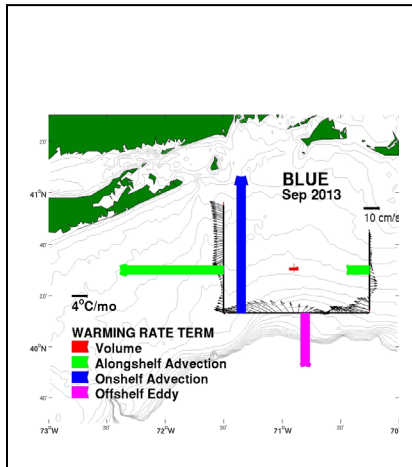


Figure 15 Cold Pool Slice Model (CPSM) results for the SNEB (glider Blue) region. The advective temperature transport (in units of warming rate) vectors are averages of the leg-cumulative products of the glider-measured temperatures and the leg-normal velocity components.

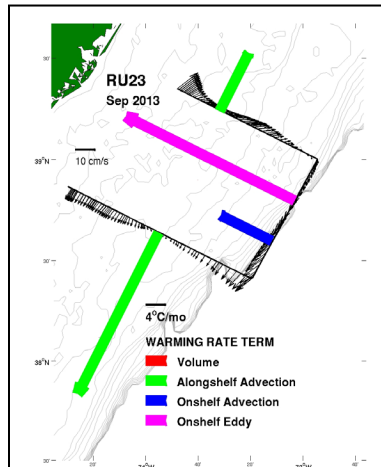


Figure 16 Cold Pool Slice Model (CPSM) results for the New Jersey shelf (glider RU23) region. The advective temperature transport (in units of warming rate) vectors are averages of the leg-cumulative products of the glider-measured temperatures and the leg-normal velocity components.

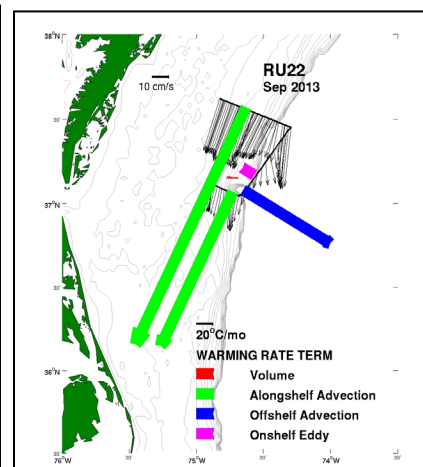
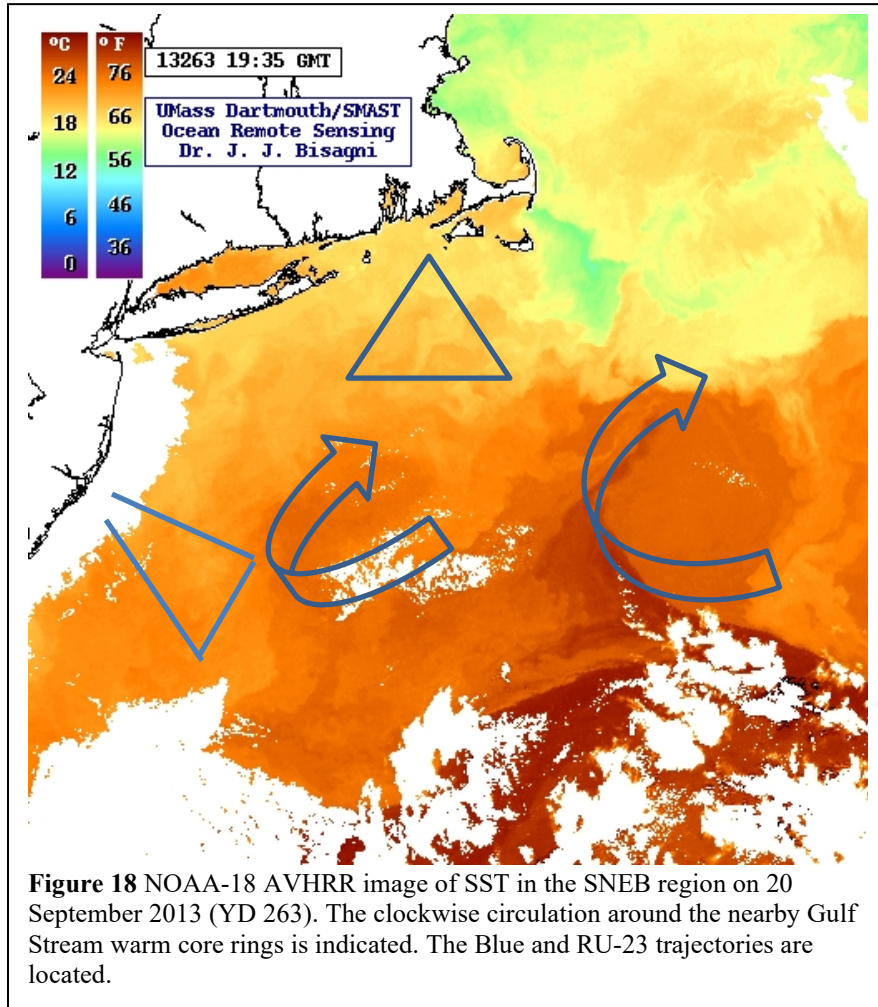


Figure 17 Cold Pool Slice Model (CPSM) results for the Maryland shelf (glider RU22) region. The advective temperature transport (in units of warming rate) vectors are averages of the leg-cumulative products of the glider-measured temperatures and the leg-normal velocity components.



VI. Summary of Findings

We generally find that a multi-glider’s eye view of the MAB Cold Pool reveals a more time-space variable habitat than previously known. While, the general warming rate of 1°C per month found in the 2007 glider observations was known, the September 2013 simultaneous observations showed a spatial gradient in that warming rate; a least in September (2013). The Cold Pool Slice Model applied to different sectors of the MAB in the same month revealed for example, the northeastern SNEB region of the MAB has a warming rate of 0.58°C in a 30.25-day month ($+ 0.22 \times 10^{-6} \text{ }^\circ\text{C/s}$). This contrasted with the much smaller New Jersey sector warming rate of 0.03 °C per month and the larger Maryland sector warming rate of 1.07°C per month. The Cold Pool Slice Model results revealed that a different set of processes prevailed in each sector. The common findings throughout the MAB that the (a) processes were more important at the open shelf – slope sea boundary and (b) upper layer warming of the Cold Pool was least important at least on the time-scale of months (September in particular).

We found that there were important differences among the sectors. With this set of observations, the SNEB sector appeared to be most vulnerable to the influence of Gulf Stream warm core rings. The NJ sector seemed to be the coldest in September with a negligible warming rate. The

most robust warming rate was in the MD sector. Perhaps more importantly it was where a substantial portion of the long-shelf flow of Cold Pool waters was robustly advected offshore.

The overall SNEB sector's *warming rate* ($0.57^{\circ}\text{C}/\text{mo}$) results because the *cooling* effects of the divergence of long-shelf flow plus the seaward eddy temperature transport was just exceeded by the onshelf advection (cross-SBF) of warm water across the seaward boundary (see [Figure 15](#)). The onshelf warm water advection was part of the GS warm core ring's contribution.

The overall New Jersey sector's negligible *warming rate* ($0.02^{\circ}\text{C}/\text{mo}$) is an order of magnitude smaller than that in the other MAB sectors during Sep. 2013 (see [Figure 16](#)). This minimum warming was maintained by a near-balance between the robust *cooling* associated with the divergence of long-shelf advective temperature transport and the robust *warming* of the onshelf eddy temperature transport. The onshelf advective temperature transport was less important to the balance than the SNEB region .

The overall Maryland sector's *warming rate* ($1.07^{\circ}\text{C}/\text{mo}$) is largest of that in the other MAB sectors during Sep. 2013 (see [Figure 17](#)). This MAB maximum warming rate is maintained through the near-balance between the robust *warming* effects of the long-shelf advective temperature transport convergence and the robust *cooling* effects from the offshelf advective temperature transports. Some of the warming Cold Pool waters were advected off the shelf through the seaward boundary; with miniscule if any eddy exchange.

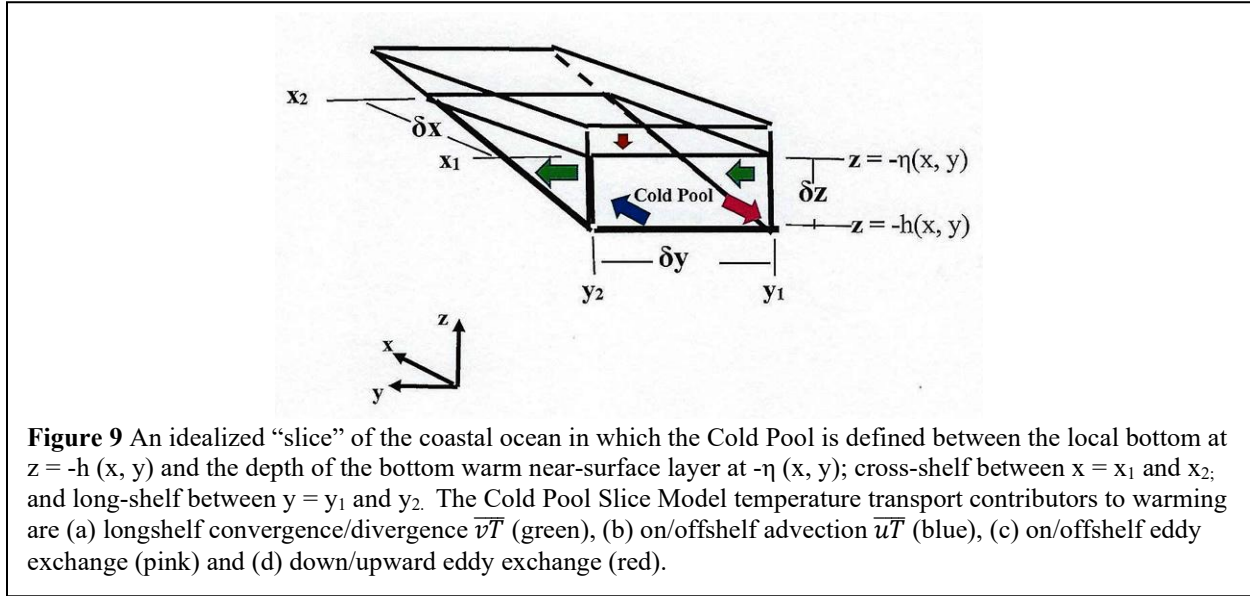
Of course, this study leaves many questions unanswered. For example, "What proportion of the Cold Pool is lost through lateral exchange before it is clearly advected off the shelf in the MD region? What mechanisms at the shelf/slope boundary operate to cause these lateral exchanges in the different sub-regions of the Mid-Atlantic Bight? The warming role of the warm core Gulf Stream ring is obvious in September 2013. Perhaps, as these warm core rings move from northeast to southwest along the MAB shelfbreak, are the most important exchange mechanism.

This study shows how gliders that poke through the shelfbreak front can gather data that can be used as demonstrated with this computational framework to address these questions. However, in order to address the questions above, the large uncertainties in these quantities, involving the glider velocities, have to be reduced in the future. But this is a start.

Appendix A: MAB Cold Pool Warming Model

The Cold Pool, which is advected from northeast to southwest through the MAB, is warmed by exchanges with longshore, offshore and upper layer waters. We consider this warming explicitly in the following model development.

Consider the longshelf flow of a model turbulent ocean flowing through a slice of the continental shelf between times $t = 0$ and $t = LOS$ (*length of series*); (see main text [Figure 9](#)).



The total flow \tilde{u}_i can be decomposed into its respective temporal mean and relative fluctuation as

$$\tilde{u}_i = \bar{u}_i(x, y, z) + u'_i(x, y, z, t), \quad (\text{A1a})$$

where the temporal mean is $\bar{\dots} = \frac{1}{LOS} \int_0^{LOS} \dots dt$ and the subscript i implies summation.

Likewise, the total temperature \tilde{T} can be decomposed as

$$\tilde{T} = \bar{T}(x, y, z) + T'(x, y, z, t). \quad (\text{A1b})$$

In these decompositions, the *temporal mean values* of the fluctuating quantities in Eq. (A1) are $\bar{T}' = 0$ and $\bar{u}'_i = 0$, respectively.

According to [Kundu \(1990\)](#), the continuity equation(s) for the *fluctuation flow* is

$$\frac{\partial u'_i}{\partial x_i} = 0 \quad (\text{A2a})$$

and the *temporal mean flow* is

$$\frac{\partial \bar{u}_i}{\partial x_i} = 0 \quad \text{or} \quad \frac{\partial \bar{u}}{\partial x} + \frac{\partial \bar{v}}{\partial y} + \frac{\partial \bar{w}}{\partial z} = 0 \quad (\text{A2b})$$

Following the [Brown \(1984\)](#), we *vertically-integrate* Eq. (A2b) between the local bottom at $z = -h(x, y)$ (rel. mean sea level at $z = 0$) and the bottom of the warm near-surface layer (top of the Cold Pool) at $z = -\eta(x, y, t)$ resulting in

$$\frac{\partial(h-\eta)}{\partial t} + \frac{\partial \hat{U}}{\partial x} + \frac{\partial \hat{V}}{\partial y} = 0, \quad (\text{A3})$$

where \hat{U} and \hat{V} are local volume transports and $(h-\eta) = h_p(x, y)$ is the spatially-dependent Cold Pool height above the bottom at $z = -h$. Thus, the *vertically-averaged* temporal mean currents are related to the transports by $U = \frac{\hat{U}}{h_p}$ and $V = \frac{\hat{V}}{h_p}$, respectively.

Assuming no temporal fluctuations in η (a spatially-dependent $z = -\eta(x, y)$ only), the continuity relation (Eq. A3) can be written as

$$\frac{\partial h_p U}{\partial x} + \frac{\partial h_p V}{\partial y} = 0. \quad (\text{A4})$$

The mean heat flux equation, according to [Landhl & Mollo-Christensen \(1992\)](#), is

$$\rho_o C_p \left(\frac{\partial \bar{T}}{\partial t} + \bar{u} \frac{\partial \bar{T}}{\partial x} + \bar{v} \frac{\partial \bar{T}}{\partial y} + \bar{w} \frac{\partial \bar{T}}{\partial z} \right) = \frac{\partial}{\partial x_i} \left(k \frac{\partial \bar{T}}{\partial x_i} - \rho_o C_p \overline{u'_i T'} \right), \quad (\text{A5})$$

where ρ_o ($= 1025 \text{ kg/m}^3$) is the reference density, C_p ($= 3900 \text{ W}_s/\text{kg}\text{-}^\circ\text{C}$) is the seawater heat capacity, and $k = \rho_o C_p \kappa$ is the molecular thermal conductivity in terms of the molecular thermal diffusivity κ ($= 1.5 \times 10^{-7} \text{ m}^2/\text{s}$).

Assuming that the turbulent heat transports $\rho_o C_p \overline{u'_i T'}$ are much larger than molecular ones and can be approximated by $K_i(-\partial \bar{T}/\partial x_i)$ in the i^{th} direction, Eq. (A5) can be written as the following *conservation of temperature equation*

$$\frac{\partial \bar{T}}{\partial t} + \bar{u} \frac{\partial \bar{T}}{\partial x} + \bar{v} \frac{\partial \bar{T}}{\partial y} + \bar{w} \frac{\partial \bar{T}}{\partial z} = \frac{\partial}{\partial z} \left(K_z \frac{\partial \bar{T}}{\partial z} \right) + \frac{\partial}{\partial y} \left(K_y \frac{\partial \bar{T}}{\partial y} \right) + \frac{\partial}{\partial x} \left(K_x \frac{\partial \bar{T}}{\partial x} \right). \quad (\text{A6})$$

In Eq. (A6), K_x , K_y , and K_z are the turbulent temperature diffusion coefficients for the inshore cross-shelf (+x), leftward along-shelf (+y) and upward (+z) temperature transport components, respectively (see main text [Figure 9](#)).

Multiplying the continuity Eq. (A2b) by \bar{T} and summing it with Eq. (A6) gives

$$\frac{\partial \bar{T}}{\partial t} + \frac{\partial \bar{u}\bar{T}}{\partial x} + \frac{\partial \bar{v}\bar{T}}{\partial y} + \frac{\partial \bar{w}\bar{T}}{\partial z} = \frac{\partial}{\partial z} \left(K_z \frac{\partial \bar{T}}{\partial z} \right) + \frac{\partial}{\partial y} \left(K_y \frac{\partial \bar{T}}{\partial y} \right) + \frac{\partial}{\partial x} \left(K_x \frac{\partial \bar{T}}{\partial x} \right) \quad (\text{A7})$$

(a1) (a2) (a3) (a4) (b) (c) (d)

We vertically-integrate *term (a4)* in Eq. (A7). Using Leibnitz's rule, with $\bar{w} = 0$ at both $z = \eta$ and $-h$, gives

$$\int_{-h(x,y)}^{-\eta(x,y)} \frac{\partial \bar{w}\bar{T}}{\partial z} dz = \int_{-h(x,y)}^{-\eta(x,y)} d\bar{w}\bar{T} = \bar{w}\bar{T} \Big|_{-h}^{-\eta} = 0. \quad (\text{A8a})$$

We also vertically-integrate *term (b)* in Eq. (A7). Using Leibnitz's rule, with the assumption of zero temperature flux at the bottom (i.e., $\partial \bar{T} / \partial z = 0$ at $z = -h$), gives

$$\int_{-h(x,y)}^{-\eta(x,y)} \frac{\partial}{\partial z} \left(K_z \frac{\partial \bar{T}}{\partial z} \right) dz = \int_{-h(x,y)}^{-\eta(x,y)} d \left(K_z \frac{\partial \bar{T}}{\partial z} \right) = K_z \frac{\partial \bar{T}}{\partial z} \Big|_{-h}^{-\eta} = K_z \frac{\partial \bar{T}}{\partial z} (-\eta) - 0. \quad (\text{A8b})$$

We also vertically integrate *terms a1, a2, a3, c, and d* in Eq. (A7) and, with the use of the short-hand notation

$$\{ \dots \dots \} \equiv \int_{-h(x,y)}^{-\eta(x,y)} \dots \dots dz,$$

and substitution of Eq. (A8), Eq. (A7) becomes

$$\left\{ \frac{\partial \bar{T}}{\partial t} + \frac{\partial \bar{u}\bar{T}}{\partial x} + \frac{\partial \bar{v}\bar{T}}{\partial y} \right\} = K_z \frac{\partial \bar{T}}{\partial z} (-\eta) + \left\{ \frac{\partial}{\partial x} \left(K_x \frac{\partial \bar{T}}{\partial x} \right) + \frac{\partial}{\partial y} \left(K_y \frac{\partial \bar{T}}{\partial y} \right) \right\}. \quad (\text{A9})$$

Then, we horizontally integrate Eq. (A9) between $x_1 \leq x \leq x_2$; and, using the short-hand notations

$$\langle \dots \dots \rangle_x \equiv \int_{x_1}^{x_2} \dots \dots dx \dots \dots \text{and } \delta_x f(x, y) = f(x_2) - f(x_1),$$

this gives

$$\left\{ \left\langle \frac{\partial \bar{T}}{\partial t} \right\rangle_x + \left(\delta_x (\bar{u}\bar{T}) + \left\langle \frac{\partial \bar{v}\bar{T}}{\partial y} \right\rangle_x \right) \right\} = \left\langle K_z \frac{\partial \bar{T}}{\partial z} (-\eta) \right\rangle_x + \left\{ \delta_x \left(K_x \frac{\partial \bar{T}}{\partial x} \right) + \left\langle \frac{\partial}{\partial y} \left(K_y \frac{\partial \bar{T}}{\partial y} \right) \right\rangle_x \right\}. \quad (\text{A10})$$

Then, we horizontally integrate Eq. (A10) between $y_1 \leq y \leq y_2$; (a) *assuming* the advective are much larger than the eddy longshelf convergences/divergences and (b) using the following short-hand notations

$[\dots \dots] \equiv \int_{y_1}^{y_2} \dots \int_{x_1}^{x_2} \dots \int_{-h(x,y)}^{-\eta(x,y)} \dots \dots dx dy dz$	volume integral
$\langle \dots \dots \rangle_y \equiv \int_{y_1}^{y_2} \dots \dots dy$	along-shelf integral
$\delta_y f(x, y) = f(y_2) - f(y_1)$	along-shelf difference
$\{ \dots \dots \}_{xz} \equiv \int_{x_1}^{x_2} \int_{-h(x,y)}^{-\eta(x,y)} \dots \dots dx dz$	cross-shelf transect integral
$\{ \dots \dots \}_{yz} \equiv \int_{y_1}^{y_2} \int_{-h(x,y)}^{-\eta(x,y)} \dots \dots dy dz$	along-shelf transect integral

$$\langle \dots \rangle \equiv \int_{y_1}^{y_2} \dots \dots \dots \int_{x_1}^{x_2} \dots \dots \dots dx dy, \quad \text{x-y plane integral}$$

Eq. (A10) becomes the Cold Pool *volume-integrated temperature conservation equation*

$$\frac{\partial \langle \bar{T} \rangle}{\partial t} = - \underbrace{\left\{ \delta_x \left(-K_x \frac{\partial \bar{T}}{\partial x} \right) \right\}}_{\text{Term-1}} - \underbrace{\left\{ \delta_x (\overline{uT}) \right\}}_{\text{Term-2}} \Big|_{yz} - \underbrace{\left\{ \delta_y (\overline{vT}) \right\}}_{\text{Term-3}} \Big|_{xz} + \underbrace{\left\langle K_z \frac{\partial \bar{T}}{\partial z} (-\eta) \right\rangle}_{\text{Term-5}}. \quad (\text{A11})$$

Each of the Eq. (A11) terms represent the following processes:

Term-1: Positive **time rate of change** of volume-integrated Cold Pool **temperature**;

Term-2: Landward (seaward) cross-shelf **eddy temperature** gain (loss);

Cold Pool height h_p goes to zero at $x = x_2$, so there is no contribution there. *Thus, the eddy temperature transport with a $-dT/dx$ across the Leg-2 transect at $x = x_1$ can **warm** the Cold Pool.*

Term-3: Landward (seaward) cross-shelf **advective temperature** gain (loss);

Cold Pool height h_p goes to zero at $x = x_2$, so there is no contribution there. *Thus, the advective temperature transport $+u\bar{T}$ across the Leg-2 transect at $x = x_1$ can **warm** the Cold Pool.*

Term-4: Net long-shelf **advective temperature** convergence/divergence gain (loss);

A convergence of the advective longshelf temperature transport can **warm** the Cold Pool.

Term-5: Downward (upward) **eddy temperature** at the top of Cold Pool gain;

Constructing the finite difference model of the Cold Pool from Eq. (A11), results in

$$\frac{\delta \langle \bar{T} \rangle}{\delta t} = \left(\overline{uT}(x_1) - K_x \frac{\partial \bar{T}}{\partial x}(x_1) \right) \delta z(x_1) \delta y + (\overline{vT}(y_1) \delta z(y_1) - \overline{vT}(y_2) \delta z(y_2)) \delta x + K_z \frac{\partial \bar{T}}{\partial z}(-\eta) \delta x \delta y \quad (\text{A12})$$

Assuming that $\delta z(y_2) = \delta z(y_1) = h_p = \delta z$ and dividing by the Cold Pool volume ($\delta x * \delta y * \delta z/2$), then Eq. (A12) can be written

$$\frac{2}{\delta x \delta y \delta z} \left(\frac{\delta \langle \bar{T} \rangle}{\delta t} \right) = \left(\overline{uT}(x_1) - K_x \frac{\partial \bar{T}}{\partial x}(x_1) \right) \frac{2}{\delta x} + (\overline{vT}(y_1) - \overline{vT}(y_2)) \frac{2}{\delta y} + K_z \frac{\partial \bar{T}}{\partial z}(-\eta) \frac{2}{\delta z} \quad (\text{A13})$$

The Cold Pool average temperature is the following

$$\frac{\delta \bar{T}_{ave}}{\delta t} = \underbrace{-\frac{2}{\delta x} K_x \frac{\partial \bar{T}}{\partial x}(x_1)}_{\text{Term-1}} + \underbrace{\frac{2}{\delta x} \overline{uT}(x_1)}_{\text{Term-2}} + \underbrace{\frac{2}{\delta y} \left((\overline{vT}(y_1)) - (\overline{vT}(y_2)) \right)}_{\text{Term-3}} + \underbrace{\frac{2}{\delta z(x_1)} K_z \frac{\partial \bar{T}}{\partial z}(-\eta)}_{\text{Term-5}} \quad (\text{A14})$$

[Table A1](#) documents how the algorithms of the terms in Eq. (14) will be estimated with glider data.

Table A1 The Eq. (A13) terms will be estimated with glider data.

	Term	Est. Term [Eq. (14)]
1	$\frac{2}{\delta x \delta y \delta z} \frac{\partial [\overline{T}]}{\partial t}$	$\frac{\delta \overline{T}_{ave}}{\delta t}$
2	$\frac{2}{\delta x \delta y \delta z} \left\{ \delta_x \left(-K_x \frac{\partial \overline{T}}{\partial x} \right) \right\}_{yz} = \frac{2}{\delta x \delta y \delta z} \int_{y_1}^{y_2} \int_{-h(x,y)}^{-\eta(x,y)} \left[-K_x \frac{\partial \overline{T}}{\partial x} (x_1) \right] dz dy$	$\frac{2}{\delta x} \left(-K_x \frac{\delta \overline{T}}{\delta x} (x_1) \right)$
3	$\left\{ \frac{2}{\delta x \delta y \delta z} \delta_x (\overline{uT}) \right\}_{yz} = \frac{2}{\delta x \delta y \delta z} \int_{y_1}^{y_2} \int_{-h(x,y)}^{-\eta(x,y)} [\overline{uT} (x_1)] dz dy$	$\frac{2}{\delta x} (+\overline{uT} (x_1))$
4	$-\left\{ \frac{2}{\delta x \delta y \delta z} \delta_y (\overline{vT}) \right\}_{xz} = \frac{2}{\delta x \delta y \delta z} \left(\int_{x_1}^{x_2} \int_{-h(x,y)}^{-\eta(x,y)} \overline{vT} (y_1) dz dx - \int_{x_1}^{x_2} \int_{-h(x,y)}^{-\eta(x,y)} \overline{vT} (y_2) dz dx \right)$	$\left(\frac{2}{\delta y} \sum_{x_1}^{x_2} \sum_{-h(x,y)}^{-\eta(x,y)} [\overline{vT} (y_1)] \right) - \left(\frac{2}{\delta y} \sum_{x_1}^{x_2} \sum_{-h(x,y)}^{-\eta(x,y)} [\overline{vT} (y_2)] \right)$
5	$\left\langle \frac{2}{\delta x \delta y \delta z} K_z \frac{\partial \overline{T}}{\partial z} (-\eta) \right\rangle = \frac{2}{\delta x \delta y \delta z} \int_{y_1}^{y_2} \int_{x_1}^{x_2} \left[\left(K_z \frac{\partial \overline{T}}{\partial z} (-\eta) \right) \right] dx dy$	$\frac{2}{\delta z} K_z \frac{\partial \overline{T}}{\partial z} (-\eta)$

Appendix B: Temperature Transport Uncertainty

The temperature transport (TT; °C-m³/s) distributions for the *lower-layer* (the sub-12°C Cold Pool layer) were estimated by multiplying the high-resolution binned 1-db temperatures and the depth-averaged (actually 3hr segment-averaged), normal-component of the velocity V_n . The V_n is derived from the components of the glider-measured ocean velocity \overline{V}_a . The glider-measured 1-db bin-averaged temperatures have a typical uncertainty ± 0.002 °C; which is $\pm 0.01\%$ of typical. Based on the [Todd et al. \(2017\)](#) comprehensive analysis of the accuracy of glider-measured currents (01 cm/s), we estimate the uncertainty shelf depth-averaged currents to be within $\pm 10\%$ (0.10). So, the uncertainty of each TT estimate is dominated by the uncertainty of depth-averaged ocean velocity normal to the transect V_n .

We seek to find the uncertainty of the transect-averaged TT, which we argue above reduces to finding the uncertainty in the transect-averaged TV_n . According to [Benedict \(1977\)](#), the *t-statistic* of the true value of the transect-averaged TV_n or $\overline{TV_n}'$ is expressed in terms of the sample mean transect average $\overline{TV_n}$ and its uncertainty limits

$$\overline{TV_n}' = \overline{TV_n} \pm t_{M-1,p} S_{\overline{TV_n}} \quad , \quad (\text{B1a})$$

where

$$S_{\overline{TV_n}} = \left[\frac{1}{M} \sum_{i=1}^M (TV_{n_i} - \overline{TV_n})^2 \right]^{1/2} \quad , \quad (\text{B1b})$$

in which M is the number of statistically-independent estimates of V_n/\bar{V}_a .

How many statistically-independent \bar{V}_a per leg depends upon their integral time-scales τ^* . We assume that the transect-normal velocities \bar{V}_n have the same τ^* s. The computed τ^* s of the two components of the detided currents \bar{V}_a for each of the three glider missions appears in [Table B1](#).

For example, there are about 50 surfacings per approximately 150-hour leg for glider Blue's 2013 SNEB mission. Since the integral time scale τ^* of the detided currents is in the range of 34 to 41 hours (see [Table B1](#)), the number of statistically-independent velocity measurements or degrees of freedom (dof or M) per leg is between 4 and 5. These dofs for the SNEB region lie between those in the NJ and MD regions of the MAB. The computed means and (after detrending the data in each leg) the standard deviations of the transect-normal velocities $\bar{T} \bar{V}_n$ are given in [Table B2](#). Thus, by Eq. (B1), the $\pm 95\%$ uncertainty limits in the respective transect-mean $\bar{T} \bar{V}_n$ are given in [Table B2](#).

Table B1 Summary of integral time scales (τ^* based on auto-correlations) for the components of the full detided currents \bar{V}_a ; and for the individual legs of the mission. The ratio of the length of series (LOS) and τ^* is the statistically-independent currents (degrees of freedom - DoF).

Glider	Vx τ^* (hr)	Vy τ^* (hr)	mean τ^* (hr)	LOS (hr)	DoF = M
BLUE	41	34	37	485	13
1				165	4
2				150	4
3				170	5
RU-23	70	49	60	396	6
1				125	2
2				125	2
3				146	2
RU-22	63	43	53	864	16
1				360	7
2				85	1
3				415	8

Table B2 The mean and standard deviation statistics of $\bar{T} \bar{V}_n$ for each leg of the different glider runs are used with Eq (B1) to compute the 95% uncertainty for the mean $\bar{T} \bar{V}_n$.

Glider	mean $\bar{T} \bar{V}_n$ (m°C/s)	SD $\bar{T} \bar{V}_n$ (m°C/s)	M	$t_{M-1,95}$	$\pm 95\%$ Uncertainty Limits (m°C/s)	$\pm 95\%$ Uncertainty Limits (°C/mo)
BLUE			13			
1	0.113	0.866	4	2.770	2.399	118.3
2	0.520	0.199	4	2.770	0.551	38.3
3	0.556	0.045	5	2.571	0.116	5.7
3-1	div 0.443				2.402	118.5
RU-23			6			
1	-0.199	0.1468	2	3.182	0.467	30.9
2	0.229	0.1011	2	3.182	0.322	15.8
3	0.548	0.1446	2	3.182	0.460	30.4
3-1	div 0.747				0.656	43.4
RU-22			17			
1	3.184	0.5195	7	2.365	1.229	119.2
2	-0.998	0.8687	2	3.182	2.764	335.2
3	2.084	0.1824	8	2.306	0.421	40.8
3-1	con - 1.100				1.299	126.0

Acknowledgments:

This research been supported in part by funding associated with several grants up through NOAA grant NA16NOS0120020 for the implementation of the Mid Atlantic Regional Association Coastal Ocean Observing System (MARACOOS). The ocean glider measurements that are the focus here were made possible through the efforts of the MARACOOS team of glider operators. We acknowledge J. Bisagni (and his collaborator Matt Oliver) who shared the images of the Gulf Stream warm core ring.

References:

- Brown, W. S., 1984. A comparison of Georges Bank, Gulf of Maine and New England Shelf Tidal Dynamics, *J. Phys. Oceanogr.*, 14(1), 145-167.
- Brown, W., O. Schofield, S. Glenn, J. Kohut and W. Boicourt, 2020. The Mid-Atlantic Bight Cold Pool, Part-1: Glider 2007 Observations (*submitted JGR Oceans*)
- Brown, W., O. Schofield, S. Glenn, J. Kohut and W. Boicourt, 2020. The Mid-Atlantic Bight Cold Pool, Part-2: Glider 2013 Observations (*submitted JGR Oceans*)
- Benedict, R.P., 1977. *Fundamentals of Temperature, Pressure and Flow Measurements*, A Wiley-Interscience Publication, John Wiley & Sons, NY,NY; pp 517.
- Groves, G.W., 1955, Numerical filters for discrimination against tidal periodicities, *Trans. Am. Geo. Union*, 36:6, 1073-1084.
- Kundu, P.K., 1990. *Fluid Mechanics*, Academic Press, Inc., Harcourt Brace Jovanovich -Pub., San Diego; pp. 432.
- Landhl, M.T., and E. Mollo-Christensen (1992). Turbulence and Random processes in Fluid Mechanics, Cambridge University Press, NY, NY; pp 168.
- Lentz, S. J., 2017. Seasonal warming of the Middle Atlantic Bight Cold Pool. *J. Geophys. Res. Oceans*, 122, 941–954, doi:[10.1002/2016JC012201](https://doi.org/10.1002/2016JC012201)
- Tremblay, K. N., 2019. Hypoxia and upwelling on the northern New Jersey coast, a September 2013 Investigation, Master's Degree Thesis, Univ. Massachusetts Dartmouth, pp 66.